

Contents lists available at ScienceDirect

Chemical Engineering Journal

journal homepage: www.elsevier.com/locate/cej





Unraveling the role of operating pressure in the rapid formation of Cu-BDC MOF via a microdroplet approach

Jianping Chen, Zan Zhu, Gustavo Monge, Wei-Ning Wang

Department of Mechanical and Nuclear Engineering, Virginia Commonwealth University, Richmond, VA 23219, USA

ARTICLE INFO

Keywords:
Aerosol dynamics
Metal-organic frameworks
Particle formation
CO₂ capture
Gas adsorption
Open metal sites

ABSTRACT

A microdroplet-based spray process has been recently developed for the synthesis of metal-organic frameworks (MOFs) which features a short processing time and scalable manner. In this process, atomized microdroplets of the MOFs precursor solution undergo well-controlled physiochemical transformations with each droplet serving as a microreactor. Droplet transformation is closely related to the flow patterns of the spray system. A conventional spray system is operated at atmospheric pressure (under the continuum flow regime). By lowering the operating pressure, the spray system is transitioned to a free-molecular flow regime, where the transport phenomena of the microdroplet become distinct due to the discrete surrounding gas. It is hypothesized that the MOFs formed under this condition could have unique morphological and structural features. Nevertheless, this topic has rarely been investigated. This work studies the formation of the copper 1,4-benzenedicarboxylate (Cu-BDC) MOF under changing flow regimes by modulating the operating pressure. Specifically, changes in crystal size, morphology, and orientation, as well as surface oxidation state, are observed with decreasing operating pressure. Heat and mass transfer calculations, accounting for the transition of flow regimes, suggest that these variations are related to different evaporation rates of the microdroplets. Our study also suggests that the dissociation of solvent molecules from Cu-BDC under sub-ambient pressure increases open metal sites which lead to a strong CO2 binding affinity. This work illustrates the synthesis of MOFs under substantially low operating pressures and offers many new opportunities in the controlled synthesis of MOFs for selective gas adsorption.

1. Introduction

Metal-organic frameworks (MOFs) emerged as an attractive class of crystalline porous material for a variety of applications [1]. In MOFs, precisely designed structures and properties are achievable by judiciously adjusting the geometry and composition of the building blocks, which endows them with great potential for applications in which preferential adsorption or molecular sieving is important, e.g., liquid and gas separation, carbon dioxide (CO2) capture and sequestration (CCS), and hydrogen storage [2]. In particular, the use of MOFs and related materials for CCS technology has revealed its potential for improving the energy efficiency of CO₂ capture systems [3,4]. The capture and concentration of low partial pressure CO2 in air and flue gas is critical to CO₂ abatement strategies [5]. With respect to enhancing the CO₂ capture performance, the modification of MOFs-based adsorbents allows the adjustment of the open metal sites [6], inorganic secondary building units [7], interactions originating from the organic functional groups [8], and the combination of MOFs with porous composites [9]

(see SI S1 for the material comparison table). Current research interests are directed toward developing materials to adsorb $\rm CO_2$ under optimal conditions yet still be economically viable at industrial scales [10]. For further information regarding MOFs in CCS the reader is referred elsewhere [11–14].

The synthesis of MOFs with tunable dimensions and properties is critical for this specific practical purpose [15]. For example, the size of MOF filler crystals can affect the performance of the CO₂ selective membrane in terms of permeability and selectivity [16]. In this regard, understanding the role of synthesis conditions for MOFs is important since it offers the ability to precisely adjust the material properties at their genesis. MOFs are conventionally synthesized via the solvothermal method typically conducted by heating the precursor solution in a closed system (Fig. 1B) [17]. However, shortcomings such as long reaction durations, inhomogeneous mixing, and limited batch processes are often associated with this method [18]. To overcome these limitations, a microdroplet-based aerosol approach, or the so-called spray route could be an appropriate strategy for synthesis of MOFs in a rapid manner

E-mail address: wnwang@vcu.edu (W.-N. Wang).

^{*} Corresponding author.

[19–21]. The spray route causes a rapid solvent phase transition upon heating the micrometer-sized aerosol droplets in a flow system, which enables the ultrafast synthesis of MOFs in seconds. In this process, atomized microdroplets of the MOF precursor solution are carried by a hot gas stream for fast solvent evaporation, nucleation, and growth of MOFs crystals (see Fig. 1A for a typical spray process) [21]. As an initial step in converting the aerosol microdroplets to MOFs crystals, solvent evaporation plays an important role in the subsequent chemical transformations within the confined microdroplets. Precursor (solvent, concentration, etc.) and process (time, temperature, pressure, etc.) parameters have strong influences on the solvent evaporation, and eventually, affect the rates of nucleation and growth of MOFs [22].

Among precursor parameters, the vapor pressure of the solvent, which affects the evaporation rate, is important for the synthesis of MOFs. Solvents with high vapor pressure were found to be responsible for synthesizing phase-pure HKUST-1 crystals by lowering the solvent evaporation rate [23]. Other than precursor parameters, the temperature is a critical process parameter because it directly affects the rates of solvent evaporation and solute diffusion, which causes changes in supersaturation ratios and affects the growth unit formation and features of the materials (Fig. 1B). As observed by He et al., [21] a high operating temperature not only decreased crystal sizes of HKUST-1 due to the increased number of seed nuclei but also affected the accessible open metal sites. Upon optimized operating temperature, suitable evaporation rates and crystallinity could be obtained, resulting in high specific surface area and large pore volume [24]. However, the temperature parameter cannot be adjusted outside the thermal stability range of target MOFs (e.g., HKUST-1 decomposes at 400 °C and above) [21]. Alternatively, the operating pressure is another important process parameter to vary the solvent evaporation rate without the thermal decomposition of MOFs.

The operating pressure is a vital process parameter controlling solvent evaporation in a flow system, such as an aerosol reactor, based on the ideal gas law. The solvothermal reactor, by contrast, has a closed environment where the solvent molecules vaporized by heat accumulate in the headspace. The differences between the two systems are highlighted in Fig. 1B. Such differences show that the operating pressure is an essential parameter to be investigated for the spray system. Our initial study suggested that the kinetics of solvent evaporation and MOF growth could be controlled by adjusting operating pressure [25], which exhibited similarities with inorganic nanoparticle formation. However, unlike inorganic materials, the crystallization of MOFs is often structurally more complex [26]. This is particularly true in the aerosol system, where the crystallization kinetics (i.e., reaction rate constants and activation energies) and crystal properties (e.g., size and structural parameters) are extremely sensitive to the local environment of the evaporative droplets (Fig. 1B) [27]. Typically, the evaporative environment of droplets is described by a continuum model under ambient pressure. However, under substantially low operating pressures, distance scales defined by the Knudsen number indicate that the transport processes occur in the free-molecular regime ($K_n \gg 1$) [28]. Droplet evaporation in this flow regime can only be described by statistical methods instead of traditional continuum fluid dynamics [29]. Hypothetically, the formation of fundamental growth unit and their self-assembly into final MOF crystals should be challenging in a discrete fluid due to weak supramolecular interactions [30]. However, the role of operating pressure in the rapid formation of MOFs is still poorly understood.

To determine the extent to which transition of the flow regime by lowering the operating pressure impacts the formation of MOFs and whether the synthetic products exhibit different physicochemical properties, we presented, for the first time, a systematic study aimed at advancing understanding of this topic. To showcase the applicability of the analysis above, we selected the copper 1,4-benzenedicarboxylate (Cu-BDC) MOF as an example. This material, initially synthesized by Mori [31], exhibits a layered crystalline structure and is promising for CO₂ selective adsorption [32]. In this work, Cu-BDC MOFs were synthesized under different pressures ranging from 50 to 760 torr. First, systematic material characterization and numerical simulations of microdroplet evaporation were conducted to assess the impact of operating pressure on material properties. Then, gas adsorption data of Cu-BDC MOFs were carefully evaluated in terms of CO2 adsorption enthalpy and selectivity. Finally, the correlation between gas adsorption behavior and material properties was given based on the key findings.

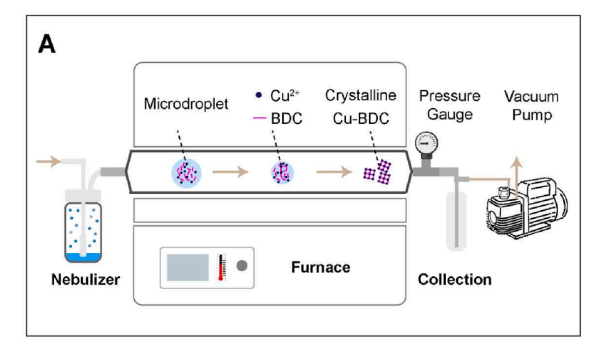
2. Materials and methods

2.1. Precursor Solution Preparation

The Cu-BDC precursor solutions were prepared by dissolving 0.4348 g of copper(II) nitrate trihydrate $(Cu(NO_3)_2\cdot 3H_2O, \geq 98\%$, Sigma-Aldrich), and 0.1994 g of benzene-1,4-dicarboxylic acid $(C_6H_4(COOH)_2, \geq 98\%$, Sigma-Aldrich, hereafter BDC) in 30 mL of N,N-dimethylformamide (HCON(CH $_3$) $_2$, $\geq 99\%$, Alfa Aesar, hereafter DMF). The chemicals were all used without further purification. The Cu-BDC precursor solutions were prepared at room temperature and stable for 8 h at least (see Figure S1).

2.2. Material Synthesis Process

As shown in Fig. 1A, Cu-BDC MOF was synthesized by using a microdroplet-based spray method. This process consisted of a carrier gas feeding system (a mass flow controller and a diffusion dryer), a Collison nebulizer, a tube furnace, a sample collector (i.e., an impinger), and an Edwards RV3 rotary vane pump for controlling the pressure. The precursor solution was first atomized by the nebulizer into microdroplets ($R_d \approx 1~\mu m$). The microdroplets were then carried by air (1.5 L min $^{-1}$) through the furnace at 200 °C. During the flying process, the microdroplets underwent solvent evaporation, nucleation, and crystallization to form final MOF products. The sample powders were collected



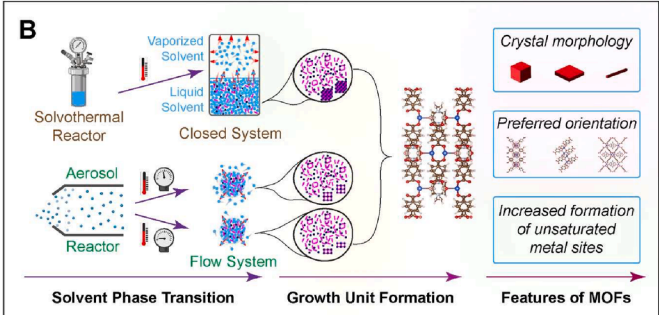


Fig. 1. (A) Schematic illustration of the synthesis of Cu-BDC in a pressure-controlled spray system. (B) Comparison of the spray method and the conventional solvothermal method in terms of crystallization mechanisms and the potential variations in properties of Cu-BDC crystals.

downstream of the furnace by using an impinger filled with DMF. During the synthesis process, the pressure inside the tube was adjusted within the range of 50 to 760 torr. In addition, bulk Cu-BDC crystals were prepared via a solvothermal method for comparison (SI S3).

2.3. Sample Washing and Activation Procedures

The as-collected samples were precipitated by centrifuging at 7000 rpm for 5 min. The separated solid was washed thoroughly with DMF to remove any non-coordinated linkers. Throughout the washing step, the MOF was resuspended into 10 mL DMF before centrifugation. This dispersion–centrifugation process was carried out twice. The purified samples were finally dried in the vacuum oven at 50 °C. Before the gas adsorption experiment, the samples were degassed at 150 °C under vacuum for 10 h.

2.4. Material Characterization

The particle size and morphology were characterized by scanning electron microscopy (SEM, Su-70, Hitachi). The structure and crystallinity of Cu-BDC were determined from powder X-ray diffraction (PXRD, X'Pert PRO, PANalytical). Surface chemistry was characterized by Fourier transform infrared (FT-IR) spectroscopy (Nicolet iS50, Thermo Scientific). The chemical state of the elements was investigated by X-ray photoelectron spectroscopy (XPS, ESCALAB 250, Thermo Scientific). Charge-correction of all spectra was performed by adjusting the adventitious carbon signal of aliphatic compounds (C-C) to 284.8 eV. CasaXPS software (v2.3.25) was used to perform all signal processing and deconvolution. Gas adsorption experiments were performed using Autosorb iQ (Quantachrome Instruments). The specific surface area and the pore size distribution were calculated from adsorption data with nitrogen collected at 77 K. Pure component gas adsorption isotherms of N_2 and CO_2 were performed at 273 K and 293 K from 0 to 1 bar.

3. Results and discussion

3.1. Morphology and Chemical Analysis

As the first demonstration of MOFs formation under different flow regimes via the microdroplet-based spray route, four Cu-BDC samples were prepared by adjusting the operating pressures in the range of 50 -760 torr. These samples will be termed hereafter by the operating pressures. Under otherwise identical synthesis conditions, the transition of flow regime was predicted to occur at the operating pressure of 90 torr when the Knudsen number equals unity. Scanning electron microscopy of the 760 torr Cu-BDC crystals under the continuum regime (Fig. 2A) reveals square lamellae exhibiting lateral dimensions in the range of 600 to 900 nm and mean thicknesses of 77 nm (i.e., aspect ratios exceeding 7.8). Interestingly, the square lamellar morphologies of the 760 torr Cu-BDC are different from their bulk counterparts which exhibit predominantly well-defined cubic MOF crystals consisting of multiple closely packed lamellae with edge dimensions ranging from 2 to 10 μm (Figure S2). Decreasing the pressure resulted in a reduction in the crystal size and the aspect ratios (Fig. 2B,C) while the sheet-like morphologies were maintained. As the pressure further decreases, the SEM image taken of the 50 torr Cu-BDC crystals (Fig. 2D) shows a needle-like morphology, which is substantially different from the sheet-like morphology associated with the continuum regime. The median crosssectional area of the crystals synthesized under 760, 250, 125, 50 torr were found to be 318,950; 53,600; 20,750 and 6,350 nm², respectively (Fig. 2E). Notably, 760 torr Cu-BDC crystals have a broad size distribution, while the size distribution of the crystals becomes more uniform as pressure decreases. Upon decreasing the operating pressure, solvent evaporation occurred more rapidly, leading to a higher supersaturation and faster nucleation rate, which gave rise to a decreased crystal size and narrower size distribution [33]. Furthermore, the area/thickness ratio of the Cu-BDC crystals was affected by pressure as well. The highest area/ thickness ratio was observed to be $\sim 10^4$ at 760 torr while the lowest was calculated to be ~ 10 at 50 torr (Fig. 2F). Thus, our synthesis strategy of decreasing the operating pressure to reach the free-molecular regime dramatically changed crystal morphology. The Cu-BDC naturally crystallizes into a two-dimensional (2D) sheet-like structure due to the

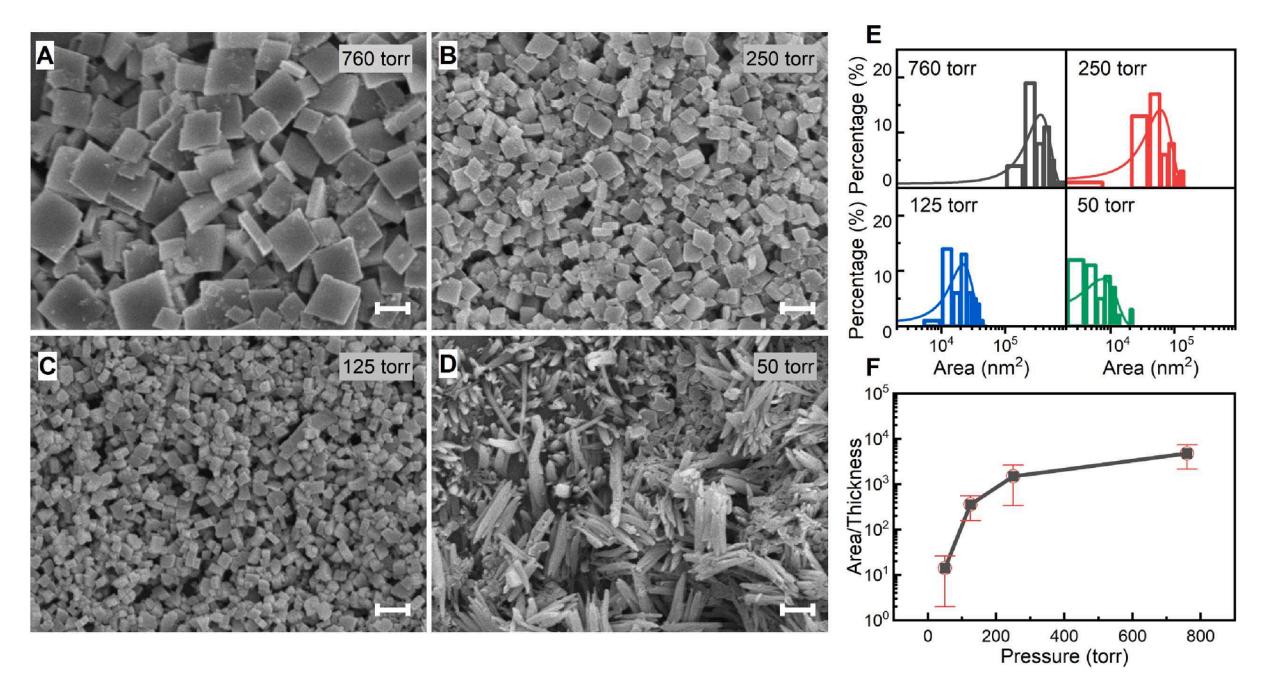


Fig. 2. (A-D) Scanning electron microscopy (SEM) images of Cu-BDC synthesized under various pressures at (A) 760 torr, (B) 250 torr, (C) 125 torr, and (D) 50 torr. Scale bars in SEM images are 500 nm. (E) Particle size distribution of Cu-BDC calculated from SEM images. (F) Evolution of the ratio between cross-section area and vertical dimension with respect to pressure. Error bars in F correspond to the standard deviations.

intrinsic structure anisotropy [34]. Due to the nature of crystallization, the high-pressure samples favor sheet-like morphologies similar to those formed by wet-chemistry methods [35]. The low-pressure condition created a faster nucleation rate, but a considerably shorter residence time [28,36], significantly affecting the crystallization process. This is particularly important for polymer crystals since they require high-molar-mass blocks to assemble into the crystalline state [37]. But this process is limited in the confined, fast-evaporating microdroplet, resulting in the morphological transition due to the limited supply of building blocks under a fast-evaporating environment.

The chemical properties of the Cu-BDC crystals were further investigated to assess the impact of the operating pressure on crystallinity. Xray diffraction of the bulk Cu-BDC showed that all the Bragg diffractions could be detected, indicative of the successful synthesis of bulk MOF structures without preferential orientation. The diffractogram of Cu-BDC structure synthesized via the spray process still has the characteristics of the predicted powder diffraction pattern based on the corresponding crystal structure (CCDC-687690, Fig. 3A), implying the successful crystallization of the Cu-BDC via the spray process despite drastically reduced reaction time. The two major peaks in the XRD pattern of bulk material correspond to the (110) and (201) planes (Figure S4) of Cu-BDC. The bulk Cu-BDC showed little crystal plane orientations as the relative intensities of all peaks were expected based on the simulated diffraction pattern of the bulk powder. In contrast, the XRD pattern of the 760 torr Cu-BDC exhibits partial preferred orientation as the relative intensity of the (201) peak starts to increase. The powder XRD data of the Cu-BDC synthesized via the spray method are similar to Cu-BDC nanosheets reported previously, although this effect of preferential orientation was enhanced when applied to nanosheets [38]. Such orientation differences can be partially attributed to the morphological changes because sheet-like crystals tend to have preferred alignment, which agrees well with the microscopy data. Likewise, the XRD patterns of Cu-BDC synthesized under lower pressures oriented along the (201) direction. Moreover, the relative intensities of the (201) crystallographic plane in the powder pattern appear to grow stronger with decreasing pressures, suggesting that the fraction of flat (201) faces of Cu-BDC increased [34]. The variations in powder XRD of Cu-BDC may be ascribed to different ways of orienting depending on the quality and size of the various particle shapes [39]. The crystalline structure of Cu-BDC consists of Cu(II) dimers with a square-pyramidal coordination geometry interconnected by benzenedicarboxylate anions. Besides the carboxylic ligands, one terminal dimethylformamide is also coordinated with the copper ions. Copper sites in Cu-BDC are ready to lose their reversibly coordinated DMF solvent upon activation [40], causing some of the peak positions in the XRD patterns of 50 torr Cu-BDC to drift. The presence of the coordinatively unsaturated copper sites (or open copper sites) may lead to shifts in the bonding environment within the Cu-BDC samples, which was investigated further with spectroscopic analysis.

We collected FT-IR spectra to examine the chemical bonding characteristics of Cu-BDC. The samples synthesized under various operating pressures showed the expected characteristic bands stemming from the organic ligands, DMF solvent, and the copper coordination groups within the frameworks (Figure S5). The observed bands for bulk Cu-BDC and the 50 torr counterpart are almost identical (Fig. 3B), indicating they have the same functional groups. The similarity shared between the measured spectra of Cu-BDC and DMF indicates that copper sites in the Cu-BDC are coordinated with DMF through the carbonyl group. Specifically, IR peaks at 1663 cm⁻¹, 1438 cm⁻¹, 1385 cm⁻¹, $1255 \,\mathrm{cm}^{-1}$, $1104 \,\mathrm{cm}^{-1}$, $882 \,\mathrm{cm}^{-1}$, $675 \,\mathrm{cm}^{-1}$ can be assigned to the DMF vibrational modes of ν s(CO), δ (CH₃), δ (CH), ν a(CN), ρ (CH₃), ν s(CN), δ(OCN), respectively [40]. Notably, after coordination of DMF to the Cu (II) center, some peaks seem to redshift a bit to higher wavenumbers compared with free DMF molecules (Fig. 3B). Besides, the -COO- group in Cu-BDC is characterized by the two bands at 1604 and 1385 cm belonging to the asymmetric and symmetric stretching modes, respectively [34]. FT-IR measurements confirmed the coordination of solvate molecules to the Cu(II) center in Cu-BDC. However, labile solvate molecules can be removed from the coordinating metal atoms to form open metal sites [41]. It is therefore likely that dissociation of coordinated solvate molecules under 50 torr will generate more open copper sites. An examination of Cu-BDC synthesized under various pressures by XPS was

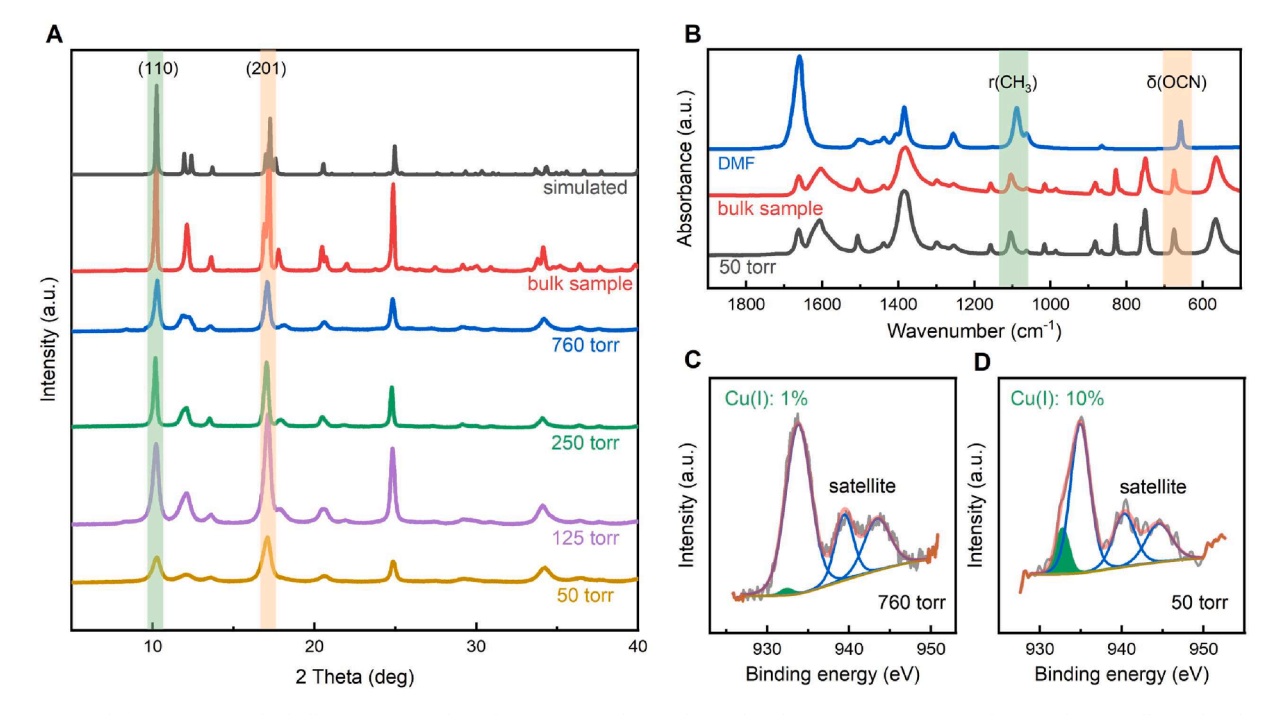


Fig. 3. (A) X-ray diffractograms of the bulk Cu-BDC sample and Cu-BDC samples synthesized under various pressure conditions. The crystallographic data used to simulate the powder diffraction pattern were obtained from the Cambridge Crystallographic Data Centre (CCDC-687690). (B) FT-IR spectra of the two Cu-BDC samples and DMF. Highlighted regions show the shift of IR peaks upon DMF coordination. (C-D) The Cu2p spectrum changes based on the %Cu(I) in the probed area of Cu-BDC under different operating pressures. The spectra are linear combinations of Cu(I) (green) and Cu(II) (blue) contributions.

performed to elucidate the chemical state information.

We found that all the Cu-BDC samples have similar elemental compositions, as shown in Figure S6, with the main differences being changes in the surface oxidation state of copper. Based on the elemental components found, high-resolution scans were collected, and the Cu2p spectra for the 760 and 50 torr samples are shown in Fig. 3C,D. The presence of Cu(II) can be found in Cu2p spectra at a characteristic binding energy of 933.8 eV. In addition to the main 2p_{3/2} peak, the wellknown shake-up satellite at roughly 944 and 940 eV can also validate the presence of Cu(II) species [42]. Shake-up peaks occur when the kinetic energy of the emitted photoelectron is reduced, which can be seen at higher binding energy than the main photoelectron line [42]. The total intensity of Cu(II) species is represented in the combination of the signals from the direct and shaken-up photoemission. The main emission line also contains the Cu(I) contribution identified by the characteristic peak at 932.4 eV [43]. The oxidation state of copper at the surface of the 50 torr Cu-BDC (Fig. 3D) was different from the 760 torr sample (Fig. 3C), evidenced by a large Cu(I) peak derived from the curve fitting results of the Cu2p XPS spectrum, in agreement with the expectation that oxidation state of copper can be reduced through dissociation of the coordinated DMF molecules. In the 760 torr Cu-BDC, the percentage of Cu(I) was identified to be 1% suggesting that copper was nearly all divalent Cu(II) species when coordinated with organic linkers (i.e., BDC) [34]. However, in the 50 torr Cu-BDC, the percentage of Cu(I) was 10%, which suggests that low operating pressure resulted in changes in the coordination environment of copper. The observed variation in the oxidation state of copper in Cu-BDC suggests that DMF molecules are more likely to dissociate from the copper sites under low operating pressures, which can give rise to differing surface characteristics.

Collectively, the results demonstrate that the crystal size, morphology, and orientation, as well as surface oxidation state of Cu-BDC, are strongly dependent on the operating pressure in an aerosol reactor. This suggests that changes in droplet evaporation induced by pressure variations are the major cause. Therefore, it will be necessary to conduct a numerical simulation of microdroplet evaporation accounting for the transition of flow regime to understand the material formation process.

3.2. Droplet Evaporation Modeling

Evaporation of aerosol droplets of MOF precursor inside the furnace is simulated under various operating pressures. Under atmospheric pressure, fluid dynamics of aerosol droplets can be described as a continuum flow because the droplet diameter is much larger than the mean free path of the surrounding gas. Aerosol dynamics practically transition from continuum to the free-molecular flow regime. Specifically, the Knudsen number $(K_n=2\lambda/d_p)$ relates the mean free path of gas molecules (λ) with the particle dimensions (d_p) and identifies free-molecular flow by $K_n\geq 1$. The transition of flow regime will occur if local pressure is reduced further. For example, if the local pressure reduces to 50 torr, the mean free path of DMF molecules is about 2 μ m, and the mean aerosol droplet radius in our aerosol system is about 1 μ m. Therefore, the droplet evaporation under such conditions must be modeled differently for the continuum regime.

In this modeling, we made some necessary assumptions. (1) Aerosol droplets contain DMF solvent only, which are monodisperse and have an initial radius of 1 μ m. (2) The characteristic time to reach thermal equilibrium (R_d^2/α) , where α is the thermal diffusivity) is in the order 10^{-6} s for $R_d=1$ μ m, which is much shorter than the evaporation time. Also, the Biot number is smaller than 0.1 for the evaporation stage; therefore, the temperature inside a droplet is uniform and the thermal gradient applies only to the droplet surface. (3) The Kelvin effect is negligible because the droplet size is much larger than 0.1 μ m. (4) Evaporation of DMF droplets is the only phenomenon responsible for mass and heat transfer. Droplet diffusion, coagulation, thermophoresis, and chemical

reactions are not important. (5) Other necessary details are provided in **SI** S7.

Solvent evaporation of aerosol droplets in a heated flow reactor is modeled as a function of reactor wall temperature, reactor pressure, droplet number density, and initial droplet size.

The change in droplet temperature (T_s) versus time (t) is given by solving the energy conservation equation in which the heat transfer from the surrounding air is equal to the enthalpy of vaporization and the amount of heat to cause the change in droplet temperature:

$$\left(\frac{dT_s}{dt}\right)_{ct} = \frac{3}{C_D d_D} \left[\frac{2h_s}{\rho_D} (T - T_s) + H_L \frac{dd_D}{dt}\right]$$
 (1)

$$\left(\frac{dT_s}{dt}\right)_{fm} = \frac{3}{C_p d_p} \left[\frac{P\overline{C}}{\rho_n} \frac{T - T_s}{T} + H_L \frac{dd_p}{dt}\right] \tag{2}$$

where T_s is the droplet surface temperature (K), T is the reactor wall temperature (473.15 K), h_s is the coefficient of heat transfer around the droplet given by **Equation** S1 (W•m⁻²•K⁻¹), H_L is the enthalpy of vaporization for DMF (J•kg⁻¹), d_p is droplet diameter (m), and P is the air pressure (Pa). The droplet surface temperatures are given in **Equations** (1) and (2) for continuum regime (ct) and free-molecular regime (fm), respectively [44].

Theoretically, the change in droplet diameter (d_p) with time (t) can be derived from the law of mass conservation in which the mass of DMF vapor that flows through the droplet surface during a unit time interval is formulated by Fick's first law of diffusion:

$$\left(\frac{dd_p}{dt}\right) = \frac{4D_v m_1 (n - n_s)}{\rho_p d_p} \tag{3}$$

where D_v is the diffusion coefficient of DMF vapor calculated by **Equation** S2 (m²/s), m_1 is the molecular mass of DMF (kg), n is the volume number density of DMF vapor (1 m⁻³). n_s is the volume number density of DMF vapor at the droplet surface (1 m⁻³) by **Equation** S3. ρ_p is the density of DMF (kg/m³) [45].

By accounting for the increase in DMF vapor density by droplet evaporation, the growth rate of DMF vapor number density over time (dn/dt) is.

$$\left(\frac{dn}{dt}\right)_{ct} = 2\pi d_p D_v N_0(n_s - n) \tag{4}$$

$$\left(\frac{dn}{dt}\right)_{fm} = \frac{\pi d_p^2 \overline{C} N_0}{4} (n_s - n) \tag{5}$$

$$\overline{C} = \sqrt{\frac{8k_BT}{\pi m}}.$$
(6)

where N_0 is the droplet number output of the single-jet Collison nebulizer. \overline{C} is the mean molecular speed (m/s) of DMF by **Equation** (6). **Equation** (4) gives the expression for the continuum (ct) regime, and the needed adaptation for the free-molecular (fm) regime is given in **Equation** (5) [44].

Equations (1) to (6) are coupled ordinary differential equations with initial conditions $T_s = 298.15$ K, $d_p = 2$ μm, and n = 0 m⁻³. This system of equations is solved simultaneously, and the simulation results are shown in Fig. 4. Interestingly, a distinct difference in droplet temperature evolution can be found in Fig. 4A. For the continuum regime, droplet temperature can reach thermal equilibrium within an extremely short time (i.e., milliseconds), which is beneficial for the homogeneous synthesis of MOF crystals, but can hardly be achieved in bulk solutions [21]. Notably, certain discrepancies exist between the reactor wall temperature (473.15 K) and the droplet surface temperature due to the evaporative cooling effect [28]. The equilibrium droplet temperature is found to be lower at 0.5 atm compared with 1 atm, but both are still higher than the initial droplet temperature. For the free-molecular

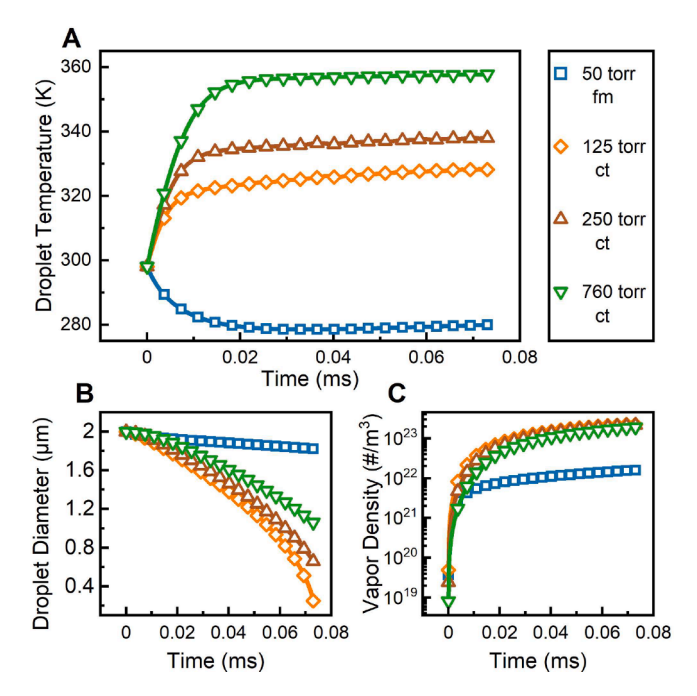


Fig. 4. (**A-C**) Evaporation kinematics of aerosol microdroplets under various pressures, characterized by the (**A**) droplet temperature T_s , (**B**) droplet diameter d_v , and (**C**) DMF vapor number density n as functions of time.

regime, the evaporative cooling effect becomes even more pronounced. At 50 torr, the droplet temperature decreases immediately. The cooling rate of microdroplets is about 6 \times 10^5 K/s under 50 torr. After the minimum temperature is approached, the droplet temperature slowly increases. The DMF droplets behaved predictably, in that they remain above the freezing point (212.2 K) in this simulation. It is important to recognize whether DMF droplets will enter the freezing zone because it can fundamentally switch the crystallization mechanism of MOFs.

As a result of droplet evaporation, the DMF vapors diffuse into the surrounding air, and hence drastically increase the DMF vapor number density. For the continuum regime, a lower operating pressure increased the diffusion coefficient of DMF vapor (Equation S2), which would accelerate the evaporation of DMF droplets and thus lead to a higher DMF vapor number density and a lower droplet diameter (Fig. 4B,C). In the free-molecular regime, ultrafast cooling of the microdroplets alters the heat and mass transfer process, creating different evaporation profiles than the continuum regime. The analytical estimation gives lower droplet temperature yet even slower evaporation of DMF droplets due to the smaller DMF vapor concentration gradient. Specifically, at the evaporation time of 0.03 ms, the droplet diameter was assessed to be 1.74 μ m under 760 torr but increased to 1.9 μ m under 50 torr (Fig. 4B). For the same duration, the droplet temperature increased by 59 K under 760 torr but dropped by 21 K under 50 torr. As shown in Figure S7, the supersaturation ratio of the solute at 0.03 ms under 50 torr was 3.5 times higher than that under 760 torr. The improved supersaturation ratio thermodynamically promotes nucleation and crystal growth [21], which is in agreement with the SEM images in Fig. 2.

Taken together, it is evident that drastic change in evaporation kinematics of precursor droplets occurs due to the pressure variations and thus gives rise to different nucleation rates. Therefore, Cu-BDC grows into various final crystalline materials with notable differences in crystal size and orientation as well as surface characteristics. These differences are surmised to impact the porosity of Cu-BDC, yielding different performances in gas adsorption.

3.3. Gas Adsorption Analysis

Fig. 5A shows the N₂ sorption isotherms (77 K) for the herein

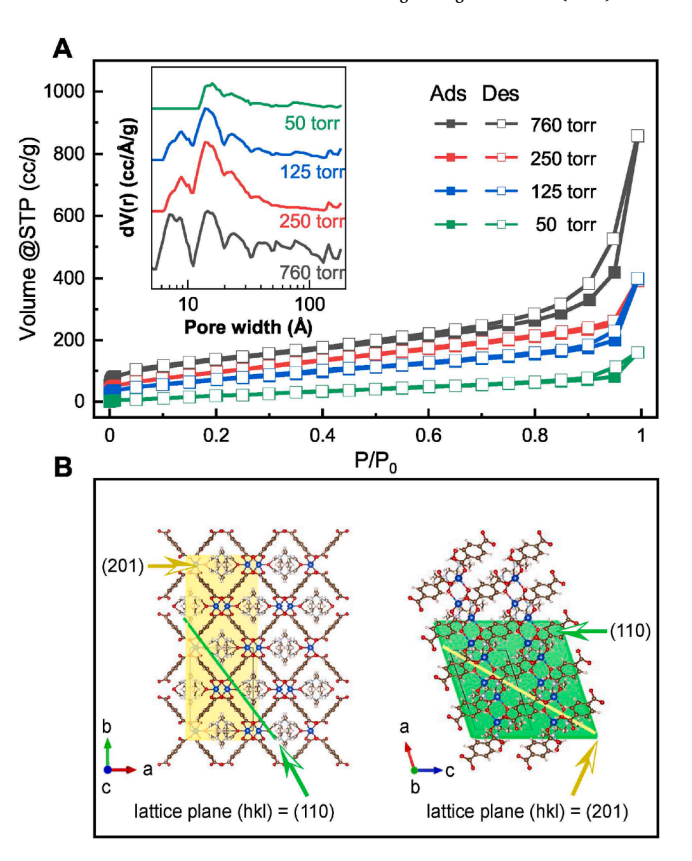


Fig. 5. (**A**) Nitrogen adsorption and desorption isotherms at 77 K for Cu-BDC synthesized under different pressures. Adsorption capacity is in units of cm³/g. Filled symbols correspond to adsorption and open symbols to desorption. The inset shows linear derivative pore size distributions of Cu-BDC calculated based on a Non-Local Density Functional Theory (NLDFT) slit-pore model. (**B**) Different views of the Cu-BDC crystalline structure showing the pore systems along (110) and (201) stacking directions. Copper, oxygen, and carbon atoms are shown in blue, red, and grey, respectively. 3D crystalline structure of Cu-BDC is shown in **Figure S4**.

synthesized Cu-BDC MOFs under various pressures. As expected, the Cu-BDC MOFs exhibited type II N2 sorption isotherms (77 K), consistent with the previous report [46]. The rapid increase in N2 adsorption isotherm on 760 torr, 250 torr, and 125 torr Cu-BDC at low relative pressure (P/P₀ < 0.01) resulted from the filling of micropores (<20 Å). Concurrently, the occurrence of hysteresis and the observed increase at relative pressures greater than 0.1 were associated with the filling of mesopores (20 to 500 Å). The calculated pore size distribution (inset of Fig. 5A), determined by the density functional theory, verifies the coexistence of micropores and mesopores. A bimodal size distribution with two peaks centered at ca. 8 and 15 Å was observed for 760 torr Cu-BDC. Effective blockage of nitrogen probe molecules from the microporous structure indicates the Cu-BDC with pore apertures smaller than the crystallographic value of 5.2 Å are obtained following our synthesis and activation procedures. Similar pore size distributions were observed in the case of 250 torr and 125 torr Cu-BDC but with fewer micropores. The adsorption isotherm of 50 torr Cu-BDC shows slow nitrogen uptake at low relative pressure, and the obtained pore size distribution suggests the elimination of micropores below 14 Å, which might be ascribed to the structural and orientational changes due to the pressure variations. MOF materials feature highly flexible pore apertures. In particular, microstructures of 2D MOFs (including thickness, preferred orientation, and interlayer structures) usually have a significant influence on their gas adsorption performance [47]. As shown in Fig. 5B, Cu-BDC MOF has a lamellar geometry that forms 2D tunnels along the (110) stacking direction, while the (201) orientation is anticipated to expose reduced

pore apertures. The ordered arrangement of apertures on the exposed (110) plane is beneficial for reducing the diffusion path lengths so that the 760 torr Cu-BDC exhibited reasonably higher $\rm N_2$ adsorption capacity than that of 50 torr Cu-BDC. The Brunauer–Emmett–Teller (BET) theory has been justified to be applicable for gas adsorption in MOFs by Snurr et.al and has been widely accepted in MOFs-related studies [48]. Analysis of the $\rm N_2$ sorption isotherms with the BET method revealed specific surface areas of 471 $\rm m^2/g$ for the 760 torr sample, comparable to those reported for related MOF structures. The obtained result for the 50 torr sample was 79 $\rm m^2/g$, indicating that the intrinsic sorption abilities of Cu-BDC were weakened with decreasing operating pressure. The bulk Cu-BDC can achieve a BET surface area of 352 $\rm m^2/g$ (see SI S9). The changes in both pore structure and surface area of the framework are attributable to the generation of MOFs with different crystal morphology and orientation under various operating pressures.

The variations in the porosity and surface properties of Cu-BDC lead to different performances in gas adsorption as demonstrated with gas adsorption isotherms in the 760 torr and 50 torr samples. The experiment of pure component gas adsorption was performed with N₂ (Fig. 6A) and CO₂ (Fig. 6B) at 273 K and 293 K from 0 to 1 bar (0 to 101.3 kPa), after which in-depth calculations were conducted to derive the isosteric enthalpy of adsorption ΔH_{ads} through virial analysis or the Clausius-Clapeyron approach [49]. The actual amount of adsorbed CO2 or N2 in a unit mass of Cu-BDC adsorbent depends on the relative pressure and the temperature together with adsorbate-adsorbent interaction energy. All experimental adsorption results followed type I isotherms. The N2 uptake capacity of 760 torr Cu-BDC at 1 bar and 273 K (0.96 mmol/g) was high than that of 50 torr Cu-BDC (0.63 mmol/g). The uptakes of N₂ at 293 K in 760 torr Cu-BDC and 50 torr Cu-BDC were much lower, accounting for 0.1 mmol/g only. Interestingly, both Cu-BDC materials showed high CO₂ uptake capacity (2.44 and 1.64 mmol/g) over N₂ at 1 bar and 273 K, suggesting their suitability for the selective removal of CO₂ from CO₂/N₂ gas mixtures (see SI S9 for the bulk Cu-BDC sample). To clarify the nature of CO₂ adsorption, we fitted the isotherms at 273 K and 293 K simultaneously in Fig. 6B with Equation S6 to calculate adsorption enthalpy based on Equation S7, which should be sufficient for comparing the interaction of the adsorbed CO2 with the Cu-BDC materials. Fig. 6C shows the isosteric enthalpy of adsorption ΔH_{ads} plotted against the amount of adsorbed CO2. The detailed calculation procedure of ΔH_{ads} can be found in SI S10. The adsorption enthalpy data show that the isosteric enthalpies for CO2 at/near-zero coverage were −28.5 and −31.9 KJ/mol for 760 torr and 50 torr Cu-BDC, respectively. These values reflect a strong effect of physisorption but remain below the chemisorption energy, which enables facile CO2 release [50]. A further positive feature of the 50 torr sample is the ratio of Henry's constant K_H for CO₂ and N₂ adsorption is 29 (see Equation S8), indicating its thermodynamic selectivity necessary for effective CO2/N2 separation [51]. The optimization of the CO₂-framework interaction is an important factor to consider when targeting high adsorption selectivity. Given that the Lewis acidic open metal sites can interact with the oxygen atoms in CO2 [52], more open copper sites in 50 torr Cu-BDC implied by XPS analysis may be attributed to the stronger adsorption affinity toward CO₂ than that of 760 torr Cu-BDC. Fig. 6C also suggests an increase in the magnitude of ΔH_{ads} at high loadings of $CO_2,$ which can be attributed to increasing CO₂-CO₂ interactions [53,54]. The comparison between the Clausius-Clapeyron approach and the virial analysis for the calculation of the adsorption enthalpy of CO2 in 50 torr Cu-BDC is presented in Fig. 6D. The Clausius-Clapeyron calculation seems to deviate from the virial result at low and high relative loadings. To conclude which approach is closer to the real values, direct calorimetric measurements are mandatory. However, few systems have been analyzed calorimetrically owing to the complexity of the experimental procedure [55].

To further evaluate the CO_2 capture selectivity, we applied the ideal adsorbed solution theory (IAST) to analyze the adsorption behavior for CO_2 from a realistic gas mixture (15% CO_2 and 85 % N_2 , mimicking flue gas composition [56,57]). The ideal adsorbed solution theory is a well-established thermodynamic model to readily predict mixed-gas

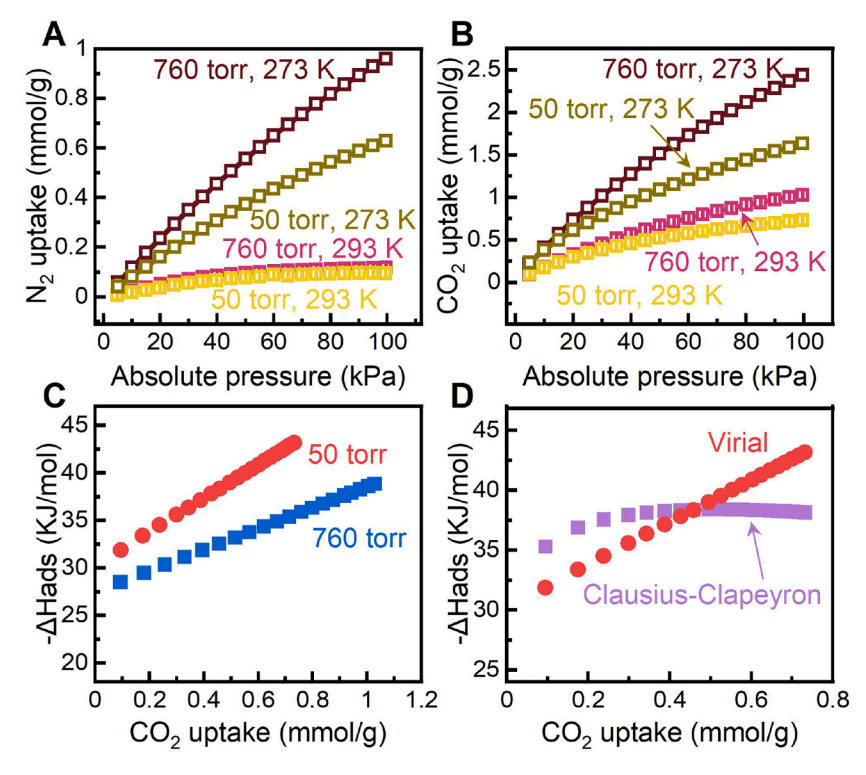


Fig. 6. (**A-B**) The pure component N₂ (**A**) and CO₂ (**B**) adsorption isotherms at 273 K and 293 K for metal—organic frameworks 760 torr Cu-BDC and 50 torr Cu-BDC. (**C**) Isosteric enthalpy of adsorption of CO₂ for 760 torr Cu-BDC and 50 torr Cu-BDC from the virial analysis of CO₂ adsorption isotherms. (**D**) Isosteric enthalpy of adsorption of CO₂ for 50 torr Cu-BDC from the virial analysis and Freundlich-Langmuir fit together with the Clausius-Clapeyron equation.

adsorption isotherms from a set of pure-component adsorption isotherms [58-60]. The accuracy of the IAST method for evaluating selectivity properties of a wide variety of porous materials has been validated by comparing it with grand canonical Monte Carlo (GCMC) simulations [61-63]. Using pure component isotherm data in Fig. 6A,B, we obtained the adsorption selectivity defined by $S_{ads} = (x_1/x_2)(y_1/y_2)$ via the IAST calculations (SI S11). As shown in Fig. 7A, different scenarios for CO₂/N₂ selectivity were found with 760 torr and 50 torr Cu-BDC MOFs owing to the variations of material properties caused by operating pressure. Remarkably, 50 torr Cu-BDC showed an increase in CO₂/N₂ selectivity at 293 K with increasing absolute gas phase pressure, while the selectivity factor at 273 K was insensitive to absolute pressure. In contrast, CO_2/N_2 selectivity factors for 760 torr sample were smaller than those of 50 torr sample at both 273 K and 293 K. Specifically, the IAST selectivity of a CO_2/N_2 binary mixture (P = 100 kPa and T = 293 K) is 29.5 for the 50 torr sample, which is higher than that of the 760 torr sample by 32% and comparable to those selectivity values of CuBDC-NO₂-a (28) [64], UiO-66(Zr)-NO₂ (26.4) [65] and MIL-125-NH₂ (27) [66]. As shown in Fig. 7B, the IAST calculation (P = 100 kPa and T =293 K) yields a CO₂ uptake of 0.84 mmol/g for the 50 torr Cu-BDC, which is five times that of the N₂ uptake. Since CO₂ and N₂ molecules have similar kinetic diameters (3.64 and 3.30 Å, respectively) [67], the observed high selectivity of the adsorbent is likely due to thermodynamic separation correlated to the differences in physical properties of the constituent gases (e.g. polarizability, quadrupole moment) which affect the isosteric heat of adsorption [68]. Finally, the IAST calculation was performed on the 50 torr Cu-BDC at $P=100\ kPa$ and $T=293\ K$ for varying CO₂ composition. Fig. 7C shows that the component uptakes follow opposite trends with increasing CO2 mole fraction. The result reveals that co-adsorption of N2 could be minimized and selectivity maximized in the 50 torr sample over the range of CO2 mole fraction

above 0.3. Because the polarizability (a) and quadrupole moment (q) of CO₂ (a = 26.5×10^{-25} cm³; $q = 4.3 \times 10^{26}$ esu $^{-1}$ cm²) are greater than those of N₂ (a = 17.6×10^{-25} cm³; $q = 1.52 \times 10^{26}$ esu $^{-1}$ cm²) [69], a high thermodynamic selectivity could be achieved through selective discrimination between the gas molecules and Lewis acidic open metal sites. Overall, these results indicate that 50 torr Cu-BDC has a strong molecular sieving effect on CO₂/N₂ mixtures, which might be attributed to the generation of coordinately unsaturated metal sites and modification of exposed pore structures.

Based on the above gas adsorption analysis, it can be concluded that Cu-BDC synthesized at a substantially low operating pressure of 50 torr exhibits decreased BET surface area, yet increased CO2/N2 selectivity. Under low operating pressure, increased diffusivity of DMF molecules (Equation S2) caused dissociation of DMF molecules from the coordinating metal atoms, generating pore-trapping species, while variations in the heat and mass transfer kinematics caused changes in crystal morphology and orientation, as suggested by results in Figs. 3 and 4. The decreased BET surface area may be ascribed to the trapped DMF molecules and the variations in the crystal structure. The open copper sites in 50 torr Cu-BDC concomitant with dissociation of DMF species potentially led to a strong binding affinity toward CO2 molecules. As suggested by many prior studies, the presence of open copper sites would increase the binding strength of CO2 adsorbate through electrostatic interactions [70-72], which would improve CO₂ adsorption selectivity. The increase in the magnitude of ΔH_{ads} together with the reduced oxidation state of copper observed with 50 torr Cu-BDC implies the existence of open copper sites. In a wider context, the described synthesis strategy in this paper offers an effective way to fine-tune the thermodynamics and kinetics of CO2 capture materials, achieved by in situ modification instead of pre- and post-synthetic modification, and thus can help devise potential adsorbent materials toward highly

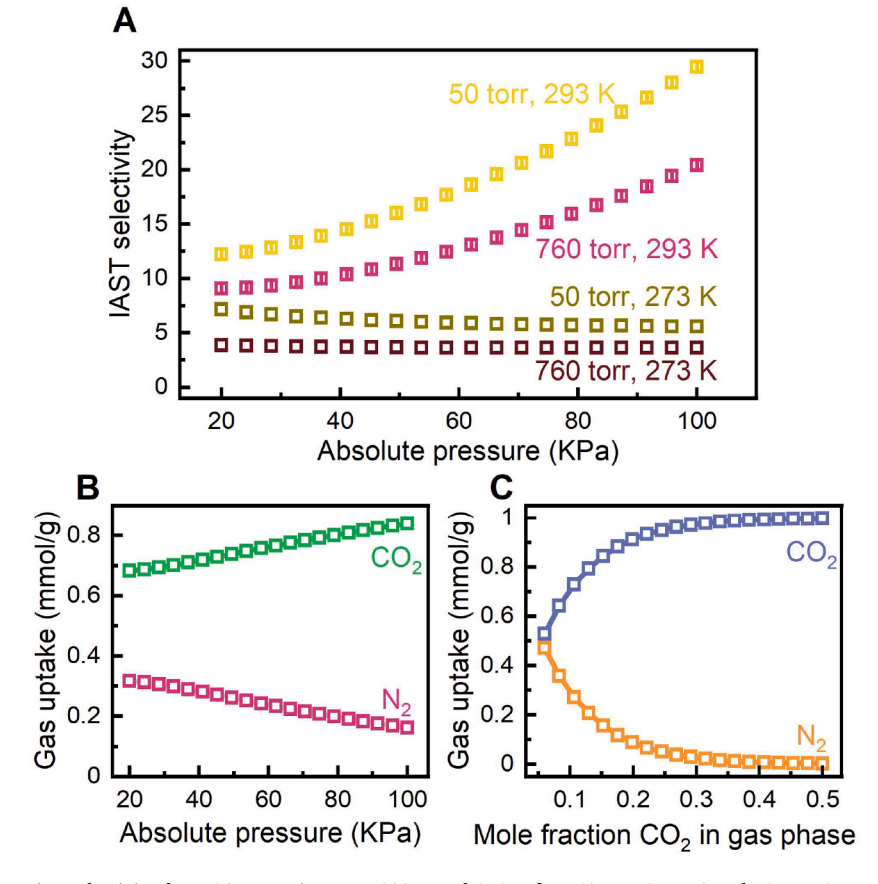


Fig. 7. (A) IAST CO_2/N_2 adsorption selectivity for a CO_2/N_2 mixture at 293 K and 273 K for 760 torr Cu-BDC and 50 torr Cu-BDC. (B) IAST-calculated mixture isotherms of CO_2 and N_2 at 293 K for 50 torr Cu-BDC. (C) IAST calculated gas uptake plotted versus mole fraction of CO_2 in the gas phase for 50 torr Cu-BDC.

selective CO_2 capture. As for deploying the MOF adsorbents for the endgoal of scalable CO_2 capture, we note that selectivity, capacity, lifetime, and many other factors need to be balanced. These considerations will be investigated more deeply in the follow-up work.

4. Conclusions

The synthesis of MOFs by a microdroplet-based spray route at substantially low operating pressures has been demonstrated for the first time. The simulation of droplet evaporation suggests that operating pressure can effectively modulate the evaporative environment and thus impact the crystal growth. The successful synthesis of a series of Cu-BDC MOFs in this study exemplifies that controlling the crystallization process of MOFs under sub-ambient pressure is a viable approach to form MOFs with excellent properties for CO₂ capture, such as massive open metal sites and high CO₂ adsorption enthalpy. The proposed method not only significantly reduces synthesis time, but also offers an effective way to fine-tune the thermodynamics and kinetics of MOFs-based adsorbents. Thus, the presented research will enrich the fundamental understanding of the synthesis of nanoscale MOFs with controlled structures and properties for adsorptive gas separation.

Declaration of Competing Interest

The authors declare that they have no known competing financial interests or personal relationships that could have appeared to influence the work reported in this paper.

Acknowledgment

Financial support from the National Science Foundation (CMMI-1727553) is gratefully acknowledged.

Appendix A. Supplementary data

Supplementary data to this article can be found online at https://doi.org/10.1016/j.cej.2022.137544.

References

- H. Li, M. Eddaoudi, M. O'Keeffe, O.M. Yaghi, Design and synthesis of an exceptionally stable and highly porous metal-organic framework, Nature 402 (6759) (1999) 276–279, https://doi.org/10.1038/46248.
- [2] R. Freund, O. Zaremba, G. Árnauts, R. Ámeloot, G. Skorupskii, M. Dincă, A. Bavykina, J. Gascon, A. Ejsmont, J. Goscianska, M. Kalmutzki, U. Lächelt, E. Ploetz, C.S. Diercks, S. Wuttke, The current status of MOF and COF applications, Angew. Chem. Int. Ed. 60 (45) (2021) 23975–24001, https://doi.org/10.1002/ anie.202106259.
- [3] J.-P. Luo, J. Zhang, N. Yin, T.-P. Wang, Z.-C. Tan, W. Han, Q. Shi, An experimental strategy for evaluating the energy performance of metal–organic framework-based carbon dioxide adsorbents, Chem. Eng. J. 442 (2022), 136210, https://doi.org/ 10.1016/j.cej.2022.136210.
- [4] A. Sinha, L.A. Darunte, C.W. Jones, M.J. Realff, Y. Kawajiri, Systems design and economic analysis of direct air capture of CO2 through temperature vacuum swing adsorption using MIL-101(Cr)-PEI-800 and mmen-Mg2(dobpdc) MOF adsorbents, Ind. Eng. Chem. Res. 56 (3) (2017) 750–764, https://doi.org/10.1021/acs.iecr.6b03887.
- [5] S.E. Renfrew, D.E. Starr, P. Strasser, Electrochemical approaches toward CO2 capture and concentration, ACS Catal. 10 (21) (2020) 13058–13074, https://doi.org/10.1021/acscatal.0c03639.
- [6] W.L. Queen, M.R. Hudson, E.D. Bloch, J.A. Mason, M.I. Gonzalez, J.S. Lee, D. Gygi, J.D. Howe, K. Lee, T.A. Darwish, M. James, V.K. Peterson, S.J. Teat, B. Smit, J. B. Neaton, J.R. Long, C.M. Brown, Comprehensive study of carbon dioxide adsorption in the metal–organic frameworks M2(dobdc) (M = Mg, Mn, Fe Co, Ni, Cu, Zn), Chem. Sci. 5 (12) (2014) 4569–4581, https://doi.org/10.1039/C4SC02064B.
- [7] P. Nugent, Y. Belmabkhout, S.D. Burd, A.J. Cairns, R. Luebke, K. Forrest, T. Pham, S. Ma, B. Space, L. Wojtas, M. Eddaoudi, M.J. Zaworotko, Porous materials with optimal adsorption thermodynamics and kinetics for CO2 separation, Nature 495 (7439) (2013) 80–84, https://doi.org/10.1038/nature11893.
 [8] O. Benson, I. da Silva, S.P. Argent, R. Cabot, M. Savage, H.G.W. Godfrey, Y. Yan, S.
- [8] O. Benson, I. da Silva, S.P. Argent, R. Cabot, M. Savage, H.G.W. Godfrey, Y. Yan, S. F. Parker, P. Manuel, M.J. Lennox, T. Mitra, T.L. Easun, W. Lewis, A.J. Blake, E. Besley, S. Yang, M. Schröder, Amides do not always work: observation of guest

- binding in an amide-functionalized porous metal-organic framework, J. Am. Chem. Soc. 138 (45) (2016) 14828–14831, https://doi.org/10.1021/jacs.6b08059.
- [9] Y. Chen, D. Lv, J. Wu, J. Xiao, H. Xi, Q. Xia, Z. Li, A new MOF-505@GO composite with high selectivity for CO2/CH4 and CO2/N2 separation, Chem. Eng. J. 308 (2017) 1065–1072, https://doi.org/10.1016/j.cej.2016.09.138.
- [10] N. McQueen, K.V. Gomes, C. McCormick, K. Blumanthal, M. Pisciotta, J. Wilcox, A review of direct air capture (DAC): scaling up commercial technologies and innovating for the future, Progress in Energy 3 (3) (2021), 032001, https://doi. org/10.1088/2516-1083/abf1ce.
- [11] Z. Sun, Y. Liao, S. Zhao, X. Zhang, Q. Liu, X. Shi, Research progress in metal–organic frameworks (MOFs) in CO2 capture from post-combustion coal-fired flue gas: characteristics, preparation, modification and applications, J. Mater. Chem. A 10 (10) (2022) 5174–5211, https://doi.org/10.1039/D1TA07856A.
- [12] M. Ding, R.W. Flaig, H.-L. Jiang, O.M. Yaghi, Carbon capture and conversion using metal-organic frameworks and MOF-based materials, Chem. Soc. Rev. 48 (10) (2019) 2783–2828, https://doi.org/10.1039/C8CS00829A.
- [13] H. Li, M.R. Hill, Low-Energy CO2 Release from metal-organic frameworks triggered by external stimuli, Acc. Chem. Res. 50 (4) (2017) 778–786, https://doi.org/ 10.1021/acs.accounts.6b00591.
- [14] L. Li, H.S. Jung, J.W. Lee, Y.T. Kang, Review on applications of metal-organic frameworks for CO2 capture and the performance enhancement mechanisms, Renew. Sustain. Energy Rev. 162 (2022), 112441, https://doi.org/10.1016/j. rser.2022.112441.
- [15] H. Xiao, Z.-X. Low, D.B. Gore, R. Kumar, M. Asadnia, Z. Zhong, Porous metal-organic framework-based filters: synthesis methods and applications for environmental remediation, Chem. Eng. J. 430 (2022), 133160, https://doi.org/ 10.1016/j.cej.2021.133160.
- [16] T. Li, Y. Pan, K.-V. Peinemann, Z. Lai, Carbon dioxide selective mixed matrix composite membrane containing ZIF-7 nano-fillers, J. Membr. Sci. 425–426 (2013) 235–242, https://doi.org/10.1016/j.memsci.2012.09.006.
- [17] A.J. Howarth, A.W. Peters, N.A. Vermeulen, T.C. Wang, J.T. Hupp, O.K. Farha, Best practices for the synthesis, activation, and characterization of metal-organic frameworks, Chem. Mater. 29 (1) (2017) 26–39, https://doi.org/10.1021/acs. chemmater.6b02626.
- [18] N. Stock, S. Biswas, Synthesis of metal-organic frameworks (MOFs): routes to various MOF topologies, Morphologies, and Composites, Chemical Reviews 112 (2) (2012) 933–969, https://doi.org/10.1021/cr200304e.
- [19] X. He, D.-R. Chen, W.-N. Wang, Bimetallic metal-organic frameworks (MOFs) synthesized using the spray method for tunable CO2 adsorption, Chem Eng J 382 (2020), 122825, https://doi.org/10.1016/j.cej.2019.122825.
- [20] A. Carné-Sánchez, I. Imaz, M. Cano-Sarabia, D. Maspoch, A spray-drying strategy for synthesis of nanoscale metal-organic frameworks and their assembly into hollow superstructures, Nat. Chem. 5 (3) (2013) 203–211, https://doi.org/ 10.1038/nchem.1569.
- [21] X. He, Z. Gan, S. Fisenko, D. Wang, H.M. El-Kaderi, W.-N. Wang, Rapid Formation of metal-organic frameworks (MOFs) based nanocomposites in microdroplets and their applications for CO2 photoreduction, ACS Appl. Mater. Interfaces 9 (11) (2017) 9688–9698, https://doi.org/10.1021/acsami.6b16817.
- [22] X. He, J. Chen, S. Albin, Z. Zhu, W.-N. Wang, Data-driven parameter optimization for the synthesis of high-quality zeolitic imidazolate frameworks via a microdroplet route, Adv. Powder Technol. 32 (1) (2021) 266–271, https://doi.org/10.1016/j. apt.2020.11.018.
- [23] J. Sun, H.T. Kwon, H.-K. Jeong, Continuous synthesis of high quality metal-organic framework HKUST-1 crystals and composites via aerosol-assisted synthesis, Polyhedron 153 (2018) 226–233, https://doi.org/10.1016/j.poly.2018.07.022.
- [24] M. Kubo, T. Saito, M. Shimada, Evaluation of the parameters utilized for the aerosol-assisted synthesis of HKUST-1, Microporous Mesoporous Mater. 245 (2017) 126–132, https://doi.org/10.1016/j.micromeso.2017.03.007.
- [25] X. He, W.-N. Wang, Pressure-regulated synthesis of Cu(TPA) (DMF) in microdroplets for selective CO2 adsorption, Dalton Trans. 48 (3) (2019) 1006–1016, https://doi.org/10.1039/C8DT03812K.
- [26] I.H. Lim, W. Schrader, F. Schüth, Insights into the molecular assembly of zeolitic imidazolate frameworks by ESI-MS, Chem. Mater. 27 (8) (2015) 3088–3095, https://doi.org/10.1021/acs.chemmater.5b00614.
- [27] M.J. Van Vleet, T. Weng, X. Li, J.R. Schmidt, In situ, time-resolved, and mechanistic studies of metal-organic framework nucleation and growth, Chem. Rev. 118 (7) (2018) 3681–3721, https://doi.org/10.1021/acs.chemrev.7b00582.
- [28] S.P. Fisenko, W.-N. Wang, I. Wuled Lenggoro, K. Okyuama, Evaporative cooling of micron-sized droplets in a low-pressure aerosol reactor, Chem. Eng. Sci. 61 (18) (2006) 6029–6034.
- [29] J. Chen, Z. Zhu, W.-N. Wang, Towards addressing environmental challenges: rational design of metal-organic frameworks-based photocatalysts via a microdroplet approach, Journal of Physics: Energy 3 (3) (2021), 032005, https://doi.org/10.1088/2515-7655/abe4a2.
- [30] A. Ramanan, M.S. Whittingham, How molecules turn into solids: the case of self-assembled metal—organic frameworks, Cryst. Growth Des. 6 (11) (2006) 2419–2421, https://doi.org/10.1021/cg0604273.
- [31] W. Mori, F. Inoue, K. Yoshida, H. Nakayama, S. Takamizawa, M. Kishita, Synthesis of New Adsorbent Copper(II) Terephthalate, Chem. Lett. 26 (12) (1997) 1219–1220, https://doi.org/10.1246/cl.1997.1219.
- [32] Z. Xin, J. Bai, Y. Shen, Y. Pan, Hierarchically micro- and mesoporous coordination polymer nanostructures with high adsorption performance, Cryst. Growth Des. 10 (6) (2010) 2451–2454, https://doi.org/10.1021/cg901520r.
- [33] K. Nakaso, K. Okuyama, M. Shimada, S.E. Pratsinis, Effect of reaction temperature on CVD-made TiO2 primary particle diameter, Chem. Eng. Sci. 58 (15) (2003) 3327–3335, https://doi.org/10.1016/S0009-2509(03)00213-6.

- [34] G. Zhan, L. Fan, F. Zhao, Z. Huang, B. Chen, X. Yang, S.-F. Zhou, Fabrication of ultrathin 2D Cu-BDC nanosheets and the derived integrated MOF nanocomposites, Adv. Funct. Mater. 29 (9) (2019) 1806720, https://doi.org/10.1002/ adfm 201806720
- [35] M. Shete, P. Kumar, J.E. Bachman, X. Ma, Z.P. Smith, W. Xu, K.A. Mkhoyan, J. R. Long, M. Tsapatsis, On the direct synthesis of Cu(BDC) MOF nanosheets and their performance in mixed matrix membranes, J. Membr. Sci. 549 (2018) 312–320, https://doi.org/10.1016/j.memsci.2017.12.002.
- [36] W. Widiyastuti, R. Balgis, F. Iskandar, K. Okuyama, Nanoparticle formation in spray pyrolysis under low-pressure conditions, Chem. Eng. Sci. 65 (5) (2010) 1846–1854, https://doi.org/10.1016/j.ces.2009.11.026.
- [37] G. Fichman, T. Guterman, J. Damron, L. Adler-Abramovich, J. Schmidt, E. Kesselman, L.J.W. Shimon, A. Ramamoorthy, Y. Talmon, E. Gazit, Spontaneous structural transition and crystal formation in minimal supramolecular polymer model, Sci. Adv. 2 (2) (2016) e1500827, https://doi.org/10.1126/sciadv.1500827.
- [38] T. Rodenas, I. Luz, G. Prieto, B. Seoane, H. Miro, A. Corma, F. Kapteijn, F.X. Llabrés i Xamena, J. Gascon, Metal-organic framework nanosheets in polymer composite materials for gas separation, Nature Mater 14 (1) (2015) 48–55.
- [39] C.F. Holder, R.E. Schaak, Tutorial on powder X-ray diffraction for characterizing nanoscale materials, ACS Nano 13 (7) (2019) 7359–7365, https://doi.org/ 10.1021/acspano.9h05157
- [40] C.G. Carson, K. Hardcastle, J. Schwartz, X. Liu, C. Hoffmann, R.A. Gerhardt, R. Tannenbaum, Synthesis and structure characterization of copper terephthalate metal-organic frameworks, Eur. J. Inorg. Chem. 2009 (16) (2009) 2338–2343, https://doi.org/10.1002/ejic.200801224.
- [41] Ü. Kökçam-Demir, A. Goldman, L. Esrafili, M. Gharib, A. Morsali, O. Weingart, C. Janiak, Coordinatively unsaturated metal sites (open metal sites) in metal–organic frameworks: design and applications, Chem. Soc. Rev. 49 (9) (2020) 2751–2798, https://doi.org/10.1039/C9CS00609E.
- [42] M.C. Biesinger, Advanced analysis of copper X-ray photoelectron spectra, Surf. Interface Anal. 49 (13) (2017) 1325–1334, https://doi.org/10.1002/sia.6239.
- [43] G. van der Laan, R.A.D. Pattrick, C.M.B. Henderson, D.J. Vaughan, Oxidation state variations in copper minerals studied with Cu 2p X-ray absorption spectroscopy, J. Phys. Chem. Solids 53 (9) (1992) 1185–1190, https://doi.org/10.1016/0022-3697(92)90037-E.
- [44] S.K. Loyalka, Mechanics of aerosols in nuclear reactor safety: a review, Prog. Nucl. Energy 12 (1) (1983) 1–56, https://doi.org/10.1016/0149-1970(83)90024-0.
- [45] Y. Xiong, T.T. Kodas, Droplet evaporation and solute precipitation during spray pyrolysis, J. Aerosol Sci. 24 (7) (1993) 893–908, https://doi.org/10.1016/0021-8502(93)90069-L.
- [46] X. He, W.-N. Wang, Synthesis of Cu-Trimesic Acid/Cu-1,4-Benzenedioic Acid via microdroplets: role of component compositions, Cryst. Growth Des. 19 (2) (2019) 1095–1102. https://doi.org/10.1021/acs.cgd.8b01606.
- [47] Y. Liu, Y. Ban, W. Yang, Microstructural engineering and architectural design of metal-organic framework membranes, Adv. Mater. 29 (31) (2017) 1606949, https://doi.org/10.1002/adma.201606949.
- [48] K.S. Walton, R.Q. Snurr, Applicability of the BET method for determining surface areas of microporous metal—organic frameworks, J. Am. Chem. Soc. 129 (27) (2007) 8552–8556, https://doi.org/10.1021/ja071174k.
- [49] A. Nuhnen, C. Janiak, A practical guide to calculate the isosteric heat/enthalpy of adsorption via adsorption isotherms in metal-organic frameworks, MOFs, Dalton Transactions 49 (30) (2020) 10295–10307, https://doi.org/10.1039/ D0DT01784A
- [50] D. Wu, J.J. Gassensmith, D. Gouvêa, S. Ushakov, J.F. Stoddart, A. Navrotsky, Direct calorimetric measurement of enthalpy of adsorption of carbon dioxide on CD-MOF-2, a green metal-organic framework, J. Am. Chem. Soc. 135 (18) (2013) 6790–6793, https://doi.org/10.1021/ja402315d.
- [51] P.Z. Moghadam, D. Fairen-Jimenez, R.Q. Snurr, Efficient identification of hydrophobic MOFs: application in the capture of toxic industrial chemicals, J. Mater. Chem. A 4 (2) (2016) 529–536, https://doi.org/10.1039/C5TA06472D.
- [52] P.D.C. Dietzel, R.E. Johnsen, H. Fjellvåg, S. Bordiga, E. Groppo, S. Chavan, R. Blom, Adsorption properties and structure of CO2 adsorbed on open coordination sites of metal-organic framework Ni2(dhtp) from gas adsorption, IR spectroscopy and Xray diffraction, Chemical Communications (41) (2008) 5125–5127, https://doi. org/10.1039/B810574J.
- [53] J.M. Simmons, H. Wu, W. Zhou, T. Yildirim, Carbon capture in metal-organic frameworks—a comparative study, Energy Environ. Sci. 4 (6) (2011) 2177–2185, https://doi.org/10.1039/C0EE00700E.

- [54] P.D.C. Dietzel, V. Besikiotis, R. Blom, Application of metal-organic frameworks with coordinatively unsaturated metal sites in storage and separation of methane and carbon dioxide, J. Mater. Chem. 19 (39) (2009) 7362–7370, https://doi.org/ 10.1039/B011242A
- [55] Z. Du, X. Nie, S. Deng, L. Zhao, S. Li, Y. Zhang, J. Zhao, Comparative analysis of calculation method of adsorption isosteric heat: Case study of CO2 capture using MOFs, Microporous Mesoporous Mater. 298 (2020), 110053, https://doi.org/ 10.1016/j.micromeso.2020.110053.
- [56] N. Huang, X. Chen, R. Krishna, D. Jiang, Two-dimensional covalent organic frameworks for carbon dioxide capture through channel-wall functionalization, Angew. Chem. Int. Ed. 54 (10) (2015) 2986–2990, https://doi.org/10.1002/ anie.201411262.
- [57] J.A. Mason, K. Sumida, Z.R. Herm, R. Krishna, J.R. Long, Evaluating metal-organic frameworks for post-combustion carbon dioxide capture via temperature swing adsorption, Energy Environ. Sci. 4 (8) (2011) 3030–3040, https://doi.org/ 10.1039/C1E601720A
- [58] A.L. Myers, J.M. Prausnitz, Thermodynamics of mixed-gas adsorption, AIChE J. 11 (1) (1965) 121–127, https://doi.org/10.1002/aic.690110125.
- [59] Y. Chen, J. Jiang, A bio-metal-organic framework for highly selective co2 capture: a molecular simulation study, ChemSusChem 3 (8) (2010) 982–988, https://doi. org/10.1002/cssc.201000080
- [60] C.M. Simon, B. Smit, M. Haranczyk, pylAST: Ideal adsorbed solution theory (IAST) Python package, Comput. Phys. Commun. 200 (2016) 364–380, https://doi.org/ 10.1016/j.cpc.2015.11.016.
- [61] S. Keskin, J. Liu, J.K. Johnson, D.S. Sholl, Testing the accuracy of correlations for multicomponent mass transport of adsorbed gases in metal—organic frameworks: diffusion of H2/CH4 mixtures in CuBTC, Langmuir 24 (15) (2008) 8254–8261, https://doi.org/10.1021/a800486f.
- [62] S. Keskin, D.S. Sholl, Assessment of a metal—organic framework membrane for gas separations using atomically detailed calculations: CO2, CH4, N2, H2 mixtures in MOF-5, Ind. Eng. Chem. Res. 48 (2) (2009) 914–922, https://doi.org/10.1021/ ie8010885.
- [63] Q. Yang, C. Zhong, Molecular simulation of carbon dioxide/methane/hydrogen mixture adsorption in metal—organic frameworks, J. Phys. Chem. B 110 (36) (2006) 17776–17783, https://doi.org/10.1021/jp062723w.
- [64] H. Cui, Y. Ye, T. Liu, Z.A. Alothman, O. Alduhaish, R.-B. Lin, B. Chen, Isoreticular microporous metal-organic frameworks for carbon dioxide capture, Inorg. Chem. 59 (23) (2020) 17143–17148, https://doi.org/10.1021/acs.inorgchem.0c02427.
- [65] W. Zhang, H. Huang, C. Zhong, D. Liu, Cooperative effect of temperature and linker functionality on CO2 capture from industrial gas mixtures in metal-organic frameworks: a combined experimental and molecular simulation study, PCCP 14 (7) (2012) 2317–2325, https://doi.org/10.1039/C2CP23839J.
- [66] S.-N. Kim, J. Kim, H.-Y. Kim, H.-Y. Cho, W.-S. Ahn, Adsorption/catalytic properties of MIL-125 and NH2-MIL-125, Catal. Today 204 (2013) 85–93, https://doi.org/ 10.1016/j.cattod.2012.08.014.
- [67] R.-B. Lin, L. Li, H. Wu, H. Arman, B. Li, R.-G. Lin, W. Zhou, B. Chen, Optimized separation of acetylene from carbon dioxide and ethylene in a microporous material, J. Am. Chem. Soc. 139 (23) (2017) 8022–8028, https://doi.org/10.1021/ jacs.7b03850.
- [68] Q. Ding, Z. Zhang, C. Yu, P. Zhang, J. Wang, X. Cui, C.-H. He, S. Deng, H., Xing, Exploiting equilibrium-kinetic synergetic effect for separation of ethylene and ethane in a microporous metal-organic framework, Science, Advances 6 (15) (2020) eaaz4322, https://doi.org/10.1126/sciadv.aaz4322.
- [69] S. Sircar, Basic research needs for design of adsorptive gas separation processes, Ind. Eng. Chem. Res. 45 (16) (2006) 5435–5448, https://doi.org/10.1021/ ie051056a
- [70] Z. Zhang, Y. Zhao, Q. Gong, Z. Li, J. Li, MOFs for CO2 capture and separation from flue gas mixtures: the effect of multifunctional sites on their adsorption capacity and selectivity, Chem. Commun. 49 (7) (2013) 653–661, https://doi.org/10.1039/ C2CC35561B
- [71] P.L. Llewellyn, S. Bourrelly, C. Serre, A. Vimont, M. Daturi, L. Hamon, G. De Weireld, J.-S. Chang, D.-Y. Hong, Y. Kyu Hwang, S. Hwa Jhung, G. Férey, High Uptakes of CO2 and CH4 in Mesoporous Metal—Organic Frameworks MIL-100 and MIL-101, Langmuir 24(14) (2008) 7245-7250. https://doi.org/10.1021/la800227x.
- [72] W.-Y. Gao, S. Palakurty, L. Wojtas, Y.-S. Chen, S. Ma, Open metal sites dangled on cobalt trigonal prismatic clusters within porous MOF for CO2 capture, Inorg. Chem. Front. 2 (4) (2015) 369–372, https://doi.org/10.1039/C4Q100240G.